Influence of Fiber Connectivity in Simulations of Cardiac BioMechanics

D Gil · R Aris · A Borras · E Ramirez · R Sebastian · M Vazquez

Abstract *Purpose:* Personalized computational simulations of the heart could open up new improved approaches to diagnosis and surgery assistance systems. While it is fully recognized that myocardial fiber orientation is central for the construction of realistic computational models of cardiac electro-mechanics, the role of its overall architecture and connectivity remains unclear. Morphological studies show that the distribution of cardiac muscular fibers at the basal ring connects epicardium and endocardium. However, computational models simplify their distribution and disregard the basal loop. This work explores the influence in computational simulations of fiber distribution at different short axis (SA) cuts.

Methods: We have used a highly parallelized computational solver to test different fiber models of ventricular muscular connectivity. We have considered two rule-based mathematical models and an own-designed method preserving basal connectivity as observed in experimental data. Simulated cardiac functional scores (rotation, torsion and longitudinal shortening) were compared to experimental healthy ranges using generalized models (rotation) and Mahalanobis distances (shortening, torsion).

D Gil, A Borras, E Ramirez
Computer Vision Center, Universitat Autonoma de Barcelona, Bellaterra, Spain
E-mail: debora,agnesba,esmitt.ramirez@cvc.uab.es

R Aris
Barcelona Super Computing Center, Barcelona, Spain
E-mail: ruth.aris@bsc.es

M Vazquez
Barcelona Supercomputing Center, BSC-CNS, Barcelona, Spain
IIIA-CSIC, Bellaterra, Spain
E-mail: mariano.vazquez@bsc.es

R Sebastian
Universitat de Valencia, Valencia, Spain

Results: The probability of rotation was significantly lower for ruled-based models (95% CI (0.13,0.20)) in comparison to experimental data (95% CI (0.23,0.31)). The Mahalanobis distance for experimental data was in the edge of the region enclosing 99% of the healthy population.

Conclusions: Cardiac electromechanical simulations of the heart with fibers extracted from experimental data produce functional scores closer to healthy ranges than rule-based models disregarding architecture connectivity.

Keywords Cardiac Electromechanical Simulations · Fiber Connectivity · Diffusion Tensor Imaging

1 Introduction

The fiber field that represents the orientation of cardiomyocytes is one of the most important factors to prescribe both electrical and mechanical properties of the myocardium. Therefore deep knowledge of its structure at the whole heart scale is a must for realistic computational modelling.

Diffusion Tensor Imaging (DTI) [20] is the reference imaging modality for the measurement of cardiac architecture [23]. To obtain fibers with the minimal accuracy required for their reconstruction, DTI should be performed on *ex-vivo* hearts. Since the experimental fiber field is not always available, mathematical models based on histological data are frequently used [22,19,16]. Among existing methods, the one described in [22] is the preferred for biomechanical simulations because it allows defining fiber orientations in both ventricles. A main advantage of mathematical models is that they can be consistently computed on any myocardial geometry. A main shortcoming is the validity of the mathematical assumptions for fully describing the complexity of cardiac fiber connectivity.

Novel studies [5,25] show that, in the near future, *in-vivo* DTI might be accurate enough for cardiac simulation of the human heart. Furthermore, fiber information could be even complemented with microstructure using synchrotron-based micro computed tomography [8]. To make the most of such multiscale data, the mesh used in simulations should accurately describe the whole myocardial geometry of each patient.

Due to its complex geometry, most simulations are run on meshes with a sub-optimal description of the heart basal region. Some models rely on a too simplified geometry obtained using a flat "top" that completely discards the basal ring. Other approaches [9] use a semi-automatic segmentation [4] manually guided by a set of key-points to locate the heart valves on the Magnetic Resonance (MR) image stack that conform the atrioventricular border. Our main concern is the uncertainty of cutting the connectivity of fibers at the basal ring. It has been reported [17] that it helps defining cardiac muscular architecture and previous works [7,2] indicate the importance of fiber orientation in electromechanical models. Since simulations were run on meshes truncated at basal level, the role cardiac architecture was not specifically explored.

This study compares the canine DTI fiber model of the John Hopkins University, JHU, public data base [1] with two synthetic models that have been generated using linear and cubic rule-based interpolation of the fibers. Our study relies on Alya [26], a computational modelling solver that allows testing many scenarios including state-of-the art multiscale models of cardiac electrophysiology and mechanics, as well as, different cardiac fiber architectures [26]. To preserve biventricular muscular architecture, we present a method for separating atria and ventricles based on the tractography of DTI data that ensures basal connectivity. Simulations are compared to experimental Tagged-MRI (TMRI) data in terms of rotation in SA planes, torsion and long axis shortening. The statistical analysis indicates that, unlike DTI-based fibers, rule-based models produce scores significantly different from healthy ranges.

2 Computational Simulation of Cardiac Biomechanics

2.1 Modelling of Cardiac Electromechanics

Governing Equations

Simulation of cardiac electromechanical propagation requires the solution of three components: electrical propagation driven by a multiscale electrophysiology model; mechanical deformation producing heart contraction; excitation-contraction coupling to link both problems together. Each component is a partial differential equation solved inside the heart volume, noted Ω_H, during a cardiac cycle. Solutions are functions of time, noted t, and volumetric coordinates, noted $\mathbf{X} = (x_1, x_2, x_3)$. Formulations for differential equations will be given using compact tensor notation. Vectors and tensors will be indicated in bold face to differentiate them from scalar quantities.

In this work, the ventricular action potential, $\mathbf{V}$, is described by a reaction-diffusion equation:

$$\nabla(D\nabla\mathbf{V}) = C_m \frac{\partial \mathbf{V}}{\partial t} + I_{ion} \tag{1}$$

for $\frac{\partial}{\partial t}$ time derivative and ∇ the divergence of a vector with respect $\mathbf{X}$. The diffusion tensor ($\boldsymbol{D}$) eigenvalues define the axial and crosswise fiber diffusion. The reactive term I_{ion} is non-linear and ruled by a set of ordinary differential equations, conforming the wave shape. In our work, we use O'Hara-Rudy cellular model [15], which reproduces protein concentrations and cellular ion channels. Finally, the constant C_m is the membrane capacitance.

The activation of the electrical stimuli is triggered by Purkinje-myocardial junctions (PMJs), which are terminal sites of the specialized cardiac conduction system distributed throughout the subendocardial layer. In this paper,

---

[1] http://gforge.icm.jhu.edu

the Purkinje network was built by a rule-based growing algorithm [21] encoding physiological constraints. This model creates the branching structure and PMJs, that connect to the tissue model at the endocardium, and included 318 PMJs in the Left Ventricle, LV, and 270 PMJs in the Right Ventricle, RV (see fig.1). The sequence of activations follows reports in the literature [14] and it starts at the lower septum, propagates to the anterior and posterior regions until the base of the papillary muscles and ends at the base of the lateral wall.
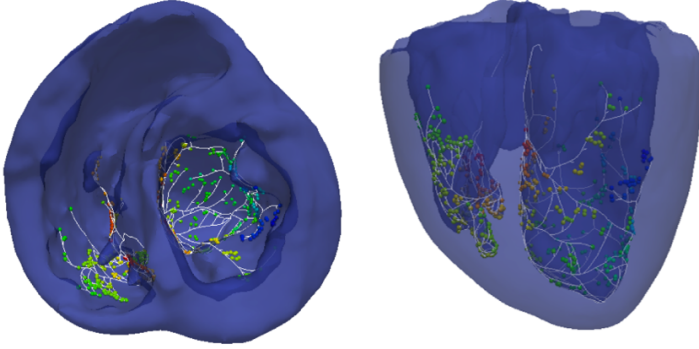
Fig. 1 Purkinje network.

Regarding the mechanical component, the myocardium is modelled as a slightly compressible material [11]. The cardiac tissue is considered hyperelastic, with an anisotropic behavior ruled by the fiber structure. Solid mechanics are described by the linear momentum balance:

$$\rho_o \frac{\partial^2 \mathbf{u}}{\partial t^2} = \frac{\partial \boldsymbol{P}}{\partial \mathbf{X}} + \rho_o \mathbf{B} \tag{2}$$

for $\mathbf{u}$ the displacement at time t, ρ_o the initial density of the body and $\mathbf{B}$ the body force. The first Piola-Kirchoff stress tensor $\boldsymbol{P}$ determines the behavior of the material and is related to the Cauchy stress tensor $\boldsymbol{\sigma}$. Following [11], $\boldsymbol{\sigma}$ is split in an active, $\boldsymbol{\sigma}_{act}$, and passive, $\boldsymbol{\sigma}_{pas}$, stress terms:

$$\boldsymbol{\sigma} = \boldsymbol{\sigma}_{pas} + \boldsymbol{\sigma}_{act}([Ca^{2+}])\boldsymbol{f} \otimes \boldsymbol{f} \tag{3}$$

for $\boldsymbol{f}$ defining the fiber direction and $\otimes$ denoting the tensor product. The passive stress is given by a transverse isotropic exponential strain energy function computed with a modified version of the Holzapfel-Ogden model [13]. The active stress governs the excitation-contraction coupling produced in the longitudinal direction of the fiber. It depends on the calcium concentration $[Ca^{2+}]$ of the cardiac cell and we compute it using the Hunter-Nash [12] model:

$$\sigma_{act} = \frac{[Ca^{2+}]^n}{[Ca^{2+}]^n + C_{50}^n} \sigma_{max}(1 + \beta(\lambda - 1)). \tag{4}$$

for λ the muscle fiber stretch, σ_{max} the maximum tensile stress for $\lambda = 1$, C_{50}^n calcium concentration for 50% of σ_{max} and β is a control constant factor. The concentration $[Ca^{2+}]$ mediates the contraction of the myocardium and is obtained from the O'Hara-Rudy cellular model [15] computed in the electrophysiology equations. Finally, mechanics-electrical feedback is assured by solving the electrophysiology problem in the deformed configuration.

Equations were solved using Alya platform [26] which simultaneously solves the electrical and mechanical problems in the same high resolution mesh. The high performance computing (HPC) simulation tool deals with large unstructured meshes [18] to account for increasing resolution and accuracy of experimental anatomical data.

Boundary Conditions

The reaction-equation monodomain model (1) assumes non-conductive medium surroundings. This is modelled as zero normal potential along Ω_H boundary:

$$\langle \mathbf{n}, \nabla(D\nabla\mathbf{V})\rangle = 0 \;\; in \;\partial\Omega_H, \tag{5}$$

for ∂ denoting the boundary of a volume, $\mathbf{n}$ the normal vector to $\partial\Omega_H$ and $\langle\cdot,\cdot\rangle$ the scalar product.

Concerning mechanics (2), the pericardium acts as a sliding surface that avoids displacements in the normal direction of the epicardium while the tangential direction remains free. The pericardium induces a displacement of ventricles in the base-apex direction and a slight torsion due to the action of the cardiac fibers. Following [6], zero normal displacement and zero tangential stress is imposed to the epicardial surface to simulate the pericardium. We use a sliding boundary condition for the pericardial region to restrict the normal displacements and allows tangential displacements.

2.2 Modelling of Cardiac Muscular Architecture

Myocardial Anatomy

In this paper, the volume Ω_H is given by the right and left ventricles excluding the atria. To apply boundary conditions the endocardium (noted End), epicardium (noted Epi) and basal (noted Bas) surfaces are also identified. We have developed a method to obtain a volume Ω_H preserving the cardiac architecture defined by fiber connectivity. Assuming more regular fiber orientation at ventricles, atria are removed considering the longest streamlines of a DTI tractography.

Given DTI tensor primary eigenvector, $\boldsymbol{f}$, tractography is computed using a 5th order Runge-Kutta-Fehlbert integration method with adaptive step size control [17]. Since the step size is adjusted using an estimated error, integration stops if $\boldsymbol{f}$ is not regular enough. Thus, the largest streamlines are inside ventricles, being atrial streamlines (without clear spatial structure) residual.

Atrial fibers are removed by a length filter and the remaining ones are used to obtain the basal surface.

Assuming a long axis aligned with the z-axis, the basal surface corresponds to points that achieve the maximal values of the ventricular fibers z-coordinate. Maximal z-values are obtained from a height volume, Z_{Bas}, of the projection of ventricular fibers onto the x-y plane. Let (xf_1, xf_2, zf_3) be the coordinates of the ventricular streamlines, then Z_{Bas} is given by:

$$Z_{Bas}(i,j,k) = \begin{cases} 1 \text{ if} & k \leq [Z_{Max}(i,j)] \\ 0 \text{ otherwise} \end{cases} \tag{6}$$

for $[\cdot]$ the integer part of a real number and $Z_{Max}(i,j) := \max_{\{[xf_1]=i,\ [xf_2]=j\}}(xf_3)$. The intersection of Z_{Bas} with an initial segmentation of the cardiac volume, noted Ω_{H0}, including the atria defines Ω_H as:

$$\Omega_H := Z_{Bas} \cap \Omega_{H0} \tag{7}$$

Fig.2 sketches our computation of Ω_H. Short fibers shown in light green are mainly present in the atria. When removed, Z_{Bas} can be computed according to maximum z-coordinates of the streamlines.

Identification of the 3 boundary surfaces (End, Epi, Bas) is based on morphological methods that compare Ω_{H0}, Ω_H and a volume, noted Ω_{H0}^f, including heart cavities. This volume is computed by a 2D filling of Ω_{H0} SA slices. Boundary surfaces are obtained from Ω_{H0}, Ω_H and Ω_{H0}^f as:

$$\begin{aligned} Epi &= \partial\Omega_{H0}^f \cap \partial\Omega_H \\ End &= \partial(\Omega_{H0}^f \setminus \Omega_{H0}) \cap \partial\Omega_H \\ Bas &= \partial\Omega_H \setminus (Epi \cup End) \end{aligned} \tag{8}$$

We extract a tetrahedral mesh of Ω_H with boundary nodes labelled according to their belonging to End, Epi, Bas in order to apply boundary conditions. The 3D tetrahedral mesh (shown in fig.2(d)) used for simulation had 89067 nodes and 450168 elements of size 0.1 cm^3.

Fiber Models

We have chosen two approaches representative of mathematical and experimental fiber models:

Mathematical Fiber Model. We use Streeter model [22] computed following [16]. For each node, fiber orientation is computed from a helix angle α that defines the rotation of the fiber along transmural direction. First we define a normalized thickness, e, using the distance from each mesh node to endocardium (d_{endo}) and epicardium (d_{epi}):

$$e = \frac{d_{endo}}{d_{endo} + d_{epi}}$$
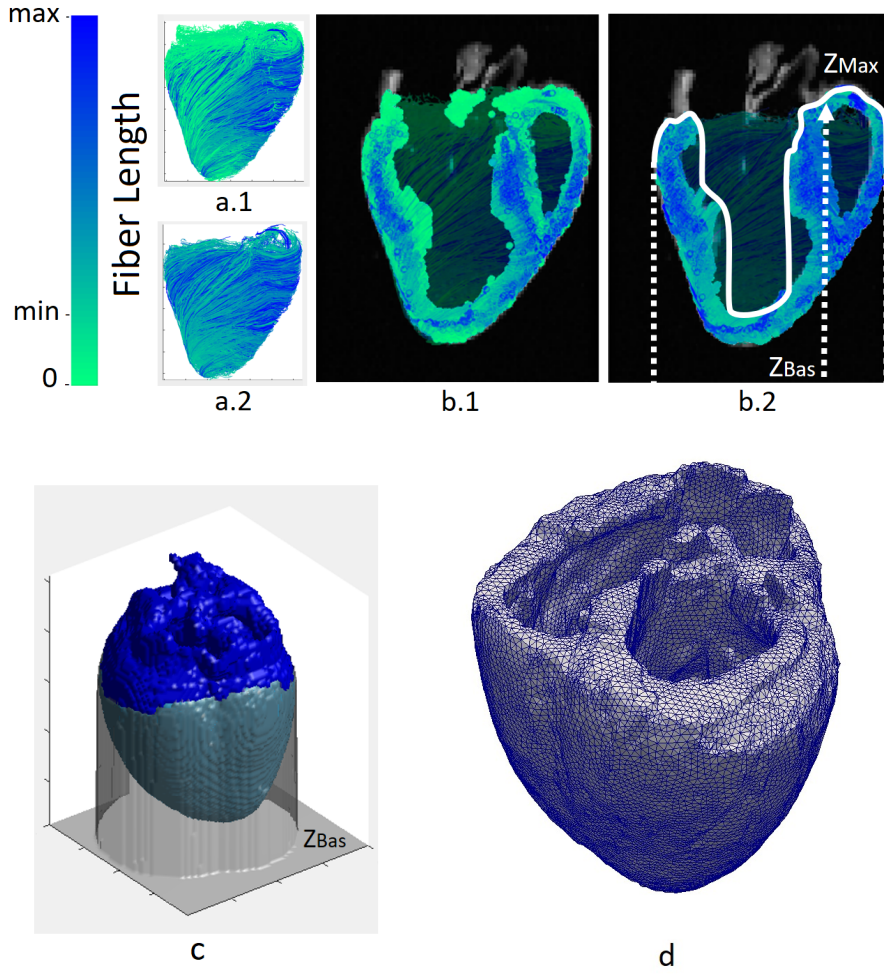
Fig. 2 Anatomy computation based on fiber density. (a.1) DTI fibers including atrial ones, (a.2) only large fibers; (b.1) All fibers shown in a LA cut, (b.2) Computation of Z_{Bas} form the large fibers; (c) Truncation Ω_{H0} following Z_{Bas}; (d) Final mesh extracted from Ω_H.

The gradient of such distance in each element is used to calculate the transmural direction. Finally, α is calculated as:

$$\alpha = R(1 - 2e)^n$$

Following [22] $R = \pi/3$ for LV and $R = \pi/4$ for RV. Like [1] we have considered a cubic ($n = 3$) and a linear ($n = 1$) model.

Experimental Fiber Model. They are defined from DTI studies as DTI tensor primary eigenvector. We have used JHU public database [2] which provides

_____

[2] http://gforge.icm.jhu.edu

volumes of eigenvectors reconstructed from DTI data and the b0 volume with
no diffusion weighting. This volume is the one we use to define Ω_H. See [10] for
additional information about JHU database including image acquisition and
post-processing methods.

Fig.3-4 show the considered fiber models: linear Streeter, ST1, cubic Streeter,
ST3, and experimental, DTI. We show streamlines reconstructed using [17] col-
ored (see side color bar) according to their elevation angle (cyan for 0°). For
better comparison of architecture, fig.4 shows a partial tractography obtained
from seeds at the mid non-septal epicardium. We also show SA and LA cuts
of volume b0. Basal Streeter fibers have 0° elevation angle and are concen-
trically arranged. Regarding DTI, streamlines elevate to the basal ring, cross
it to reach the epicardium and then trace a dense helicoid from base to apex
[24]. Such helicoid and epi-endo basal connection are better visualized in the
streamlines restricted to the non-septal LV of fig.5.
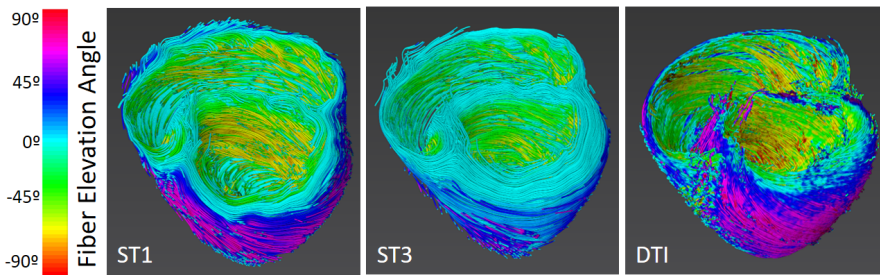
Fig. 3   Fiber models. Streeter (linear, ST1, and cubic, ST3) and DTI fibers.

3 Comparison to Experimental Data

3.1 Experimental DataSet

Simulations have been compared to experimental functional data acquired in
the MIOCARDIA project [3]. The data acquired consists in TMRI studies from
20 healthy volunteers and 3 pathological patients with different levels (mild,
medium and severe) of depressed LV function.

For the TMRI study, a Siemens Avanto 1.5 T (Erlangen, Germany) was
used. TMRI sequences were oriented in a transversal plane from the LV cov-
ering from the base to the apex. The basal slice was chosen as the first one
showing a discrete image of the LV myocardial wall below the LV outflow tract,
and the apical slice considered as the last one allowing the visualization of the
LV cavity in diastole.

---

[3] http://iam.cvc.uab.es/portfolio/cardiac-imaging-analysis/
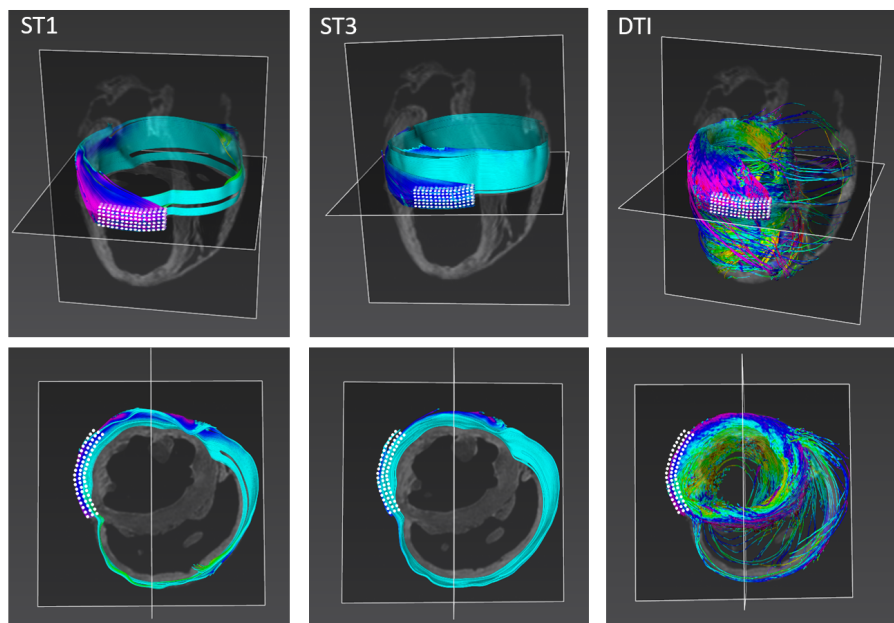
Fig. 4 Fiber models architecture from a tractography starting at the white dots.
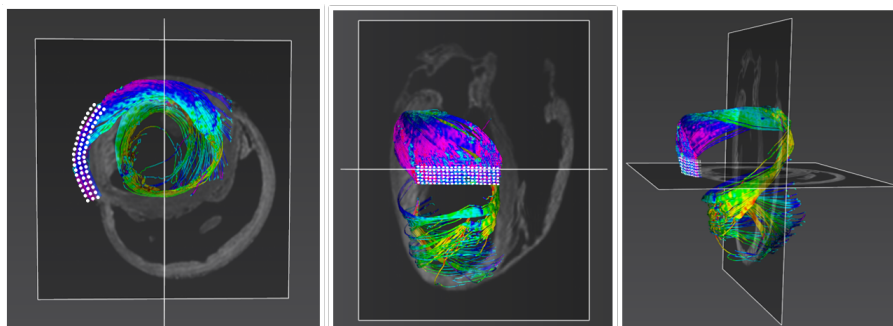
Fig. 5 DTI fibers helicoidal loop crossing the basal ring.

3.2 Functional Scores

The mechanics simulated using the different fiber models were compared to experimental data in terms of LV rotation in SA planes along the systolic cycle and absolute myocardial torsion (AMT) and left ventricular long axis longitudinal shortening (LVLS) at end-systole. These scores correlate well to cardiac function and the pair (AMT,LVLS) is discriminate of cardiac function abnormalities [3]. AMT was given by the difference between the maximum rotation at the most basal section (BMR) and at the apex (AMR) as:

$$AMT = AMR - BMR \tag{9}$$

Regarding LSLV, the distance (in mm) between the apex of the LV and the center of the basal ring at end-diastole and end-systole was computed in 2 LA oriented in 2-chamber and 4-chamber views. The longitudinal shortening on the 2-chamber (E2) and 4-chamber (E4) planes was calculated as the percentage of the reduction in the measured distances:

$$E_2 = 100 \left(1 - \frac{d_{2,1}}{d_{2,0}}\right) \qquad E_4 = 100 \left(1 - \frac{d_{4,1}}{d_{4,0}}\right) \qquad (10)$$

for $d_{2,0}$, $d_{4,0}$ distances at end-diastole and $d_{2,1}$, $d_{4,1}$ distances at end-systole. Finally, the LSLV was defined as the average:

$$LSLV = \frac{E_2 + E_4}{2} \qquad (11)$$

3.3 Statistical Analysis

Like [3], normality models for the probabilistic distribution of SA rotation, AMT and LVLS were created using the 20 healthy volunteers. These models were used to assess the likelihood of the scores computed using simulated data.

For (AMT, LVLS) we followed [3] to detect deviations in simulations from normal cases. A normality model was computed by fitting a bimodal Gaussian model to AMT and LSLV normal values. The covariance matrix of the model was used to compute the Mahalanobis distance between simulations and the Gaussian average as score of deviation from normal cases. The highest this distance is, the further from the healthy population average simulated scores are.

Concerning SA rotation, no measure of deviation from normal cases was reported in [3]. In order to quantify deviations, we computed a normality model from healthy cases. To account for non-Gaussianity in data we used the empirical density function of healthy cases. A different empirical density, labelled P_t^{SA}, was computed for each SA cut and systolic time t. The probability of simulated rotations was computed from P_t^{SA} tails as:

$$pSim^{SA} = pSim^{SA}(t) := min(P_t^{SA}(\theta \leq \theta_t^{SA}), P_t^{SA}(\theta \geq \theta_t^{SA})) \in [0,1] \quad (12)$$

for θ_t^{SA} the rotation angle obtained from the simulation. Unlike the Mahalanobis distance, $pSim^{SA}$ quantifies the similarity of SA rotation to normal cases. Low values indicate that simulated rotations are not in the ranges expected for a healthy population.

Tail probabilities (12) were statistically analyzed with R, version 3.2.5. The descriptive statistical analysis included the number of samples, the mean and the standard deviation (SD). Main analysis was performed using a generalized model with a factor for the fiber model, a factor for the SA cut and the percentage of systolic phase as adjusting factor:

$$pSim_{ijk}^{SA} = \beta_0 + \beta_1 t_{ijk} + \alpha_1 SimMod_i + \alpha_2 SA_j + \epsilon_{ijk} \qquad (13)$$

Explicative variables	Descriptive			Model		
	n	mean	SD	coeff	p-val	95% CI
Fiber Model						
DTI ($SimMod_1$)	60	0.34	0.33	1	-	(0.23,0.31)
ST1 ($SimMod_2$)	60	0.25	0.27	0.05	<0.01	(0.17,0.31)
ST3 ($SimMod_3$)	60	0.20	0.23	0.07	<0.01	(0.13,0.20)
SA Cut						
Apex (SA_1)	60	0.31	0.32	1	-	(0.25,0.34)
Mid (SA_2)	60	0.38	0.30	-0.04	0.06	(0.31,0.40)
Base (SA_3)	60	0.10	0.12	0.15	<0.01	(0.04,0.12)

**Table 1** Model for the probability of simulated rotation.

for $SimMod_i$, $i = 1, 2, 3$ indicating the fiber model used in simulations ($SimMod_1$ for the baseline DTI, $SimMod_2$ for ST1, $SimMod_3$ for ST3), and SA_j, $j = 1, 2, 3$ indicating the short axis plane (SA_1 for the reference Apex, SA_2 for Mid, SA_3 for Base). The model was adjusted using a Gamma distribution (inverse link function) for $pSim_{ijk}^{SA} + 1$. We computed model coefficients, p values for significance in main effects, and the 95% confidence intervals (CI) for $pSim^{SA}$. CIs were back transformed to the original scale for their interpretation. A p value < 0.05 was considered statistically significant.

4 Results

Simulations were run on meshes extracted from JHU study DT080803 and DT080803 b_0 volume was segmented using Otsu thresholding to obtain Ω_{H0}. The mesh of the labelled volume Ω_H had 450200 tetrahedral elements of size 0.1 cm^3. Fibers were defined from DT080803 DTI tensor and using linear and cubic Streeter models. Simulated data will be labelled "DTI", "ST1", "ST3" for data obtained using DTI-based, linear Streeter and cubic Streeter models, respectively. A total of 9 simulations were run solving Electrophysiology and mechanical deformation equations on the same mesh, to avoid instability issues and interpolation errors

Fig.6 shows simulations at end-systole in 2 LA views with the volume at end-diastole displayed in gray for comparison purposes. Streeter models, especially ST3, present an anomalous bow (indicated with red arrows) at the basal septal area.

The analysis of $pSim^{SA}$ (reported in Table 1) detected significant differences across fiber models and in the basal SA cut. According to the model, the 95% CI for $pSim^{SA}$ was decreasing in the fiber factor $SimMod$ with $(0.23, 0.31)$ for DTI, $(0.17, 0.31)$ for ST1, and $(0.13, 0.20)$ for ST3. A test comparing CIs was significant for differences between DTI and the two rule-based models ST1 (p-val=0.02) and ST3 (p-val< 0.01). Line graphs in fig.7 illustrate these comparisons. The decreasing pattern with respect systolic phase percentage is expected due to accumulation errors. Concerning SA levels, simulations were significantly worst at basal level with a 95% CI for $pSim^{SA}$ equal
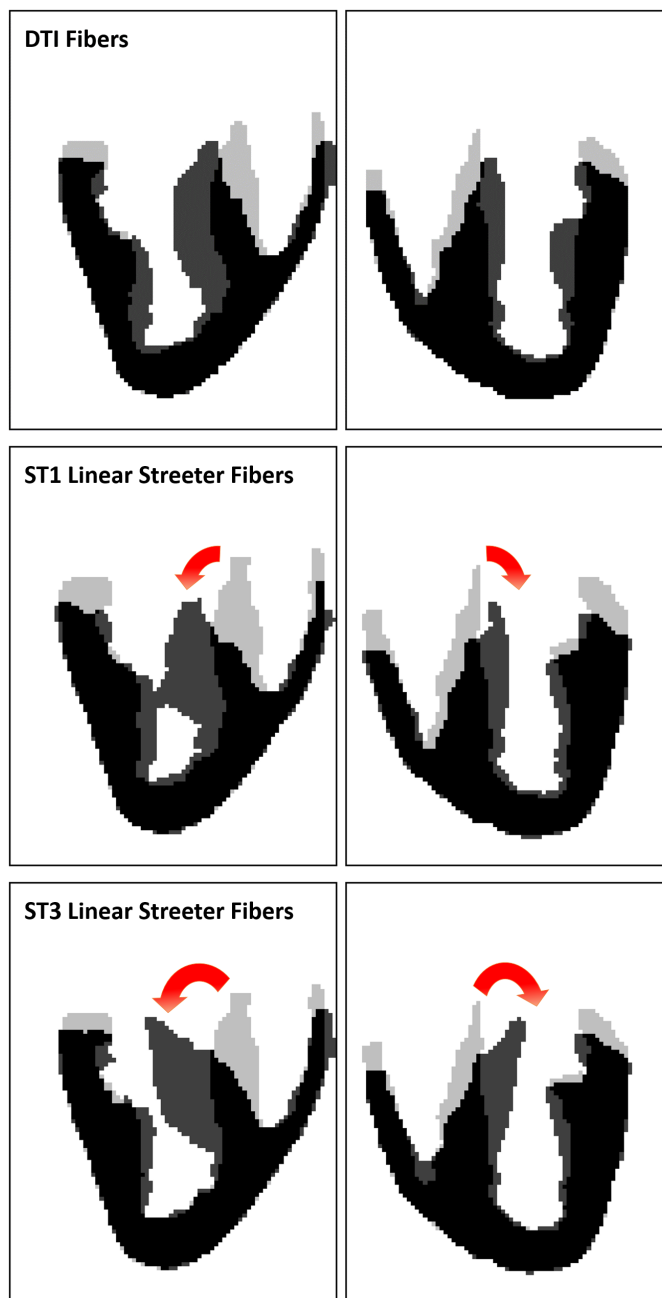
Fig. 6 Simulated motion in two different LA views at end systole.

to $(0.04, 0.12)$ in comparison to a CIs equal to $(0.31, 0.40)$ for Mid cuts and $(0.25, 0.34)$ for the Apex.
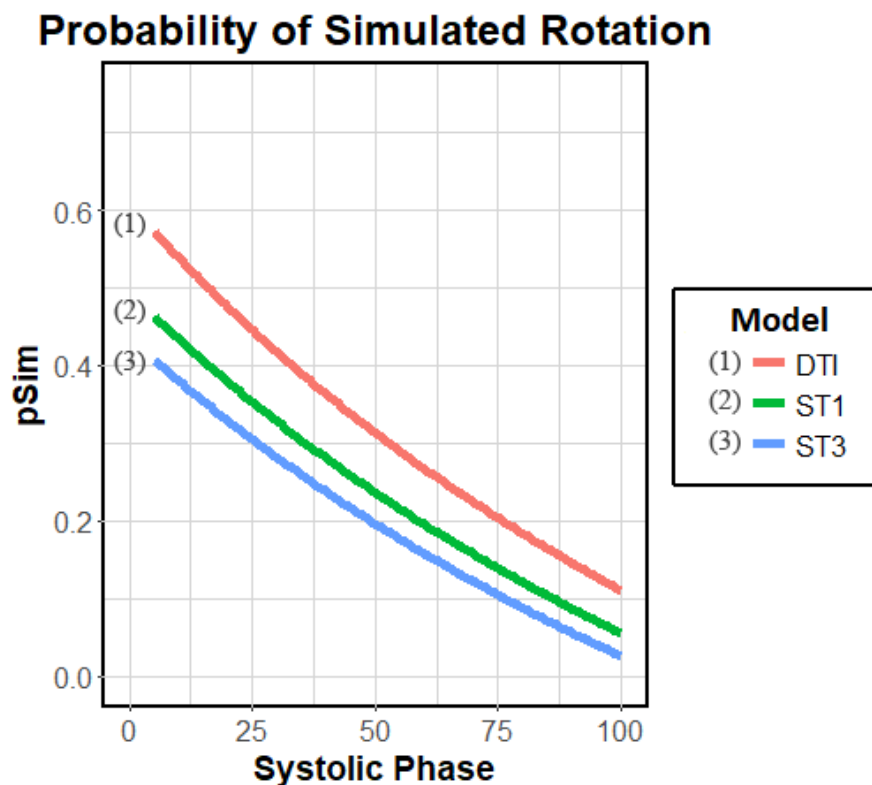
Fig. 7 Comparison of the estimated probability of rotation for each fiber model

Concerning Mahalanobis distances for (AMT, LVLS), the values for simulated data were 4.18 for DTI, 7.7 for ST1 and 8.4 for ST3, while values for pathological cases were 3.3 for the mild, 8.7 for the medium and 15.13 for the severe case. Fig.8 shows (AMT, LVLS) values for the healthy cases (blue dots), pathological ones (red crosses) and simulated data (green crosses labelled with the fiber model). To better compare to normality values, the ellipse representing the 99% of the probability density function for the healthy population is also drawn. Samples outside this ellipse have less than 1% of probability of being healthy.

5 Discussion and Conclusions

Our experiments show that DTI-simulations using a geometry especially segmented to preserve fiber architecture produce functional scores significantly closer to healthy ranges than Streeter models. Such models have a circular disposition in SA planes (fig.4) and fail to reproduce the helicoidal trace and epi-endo basal connection of experimental data.
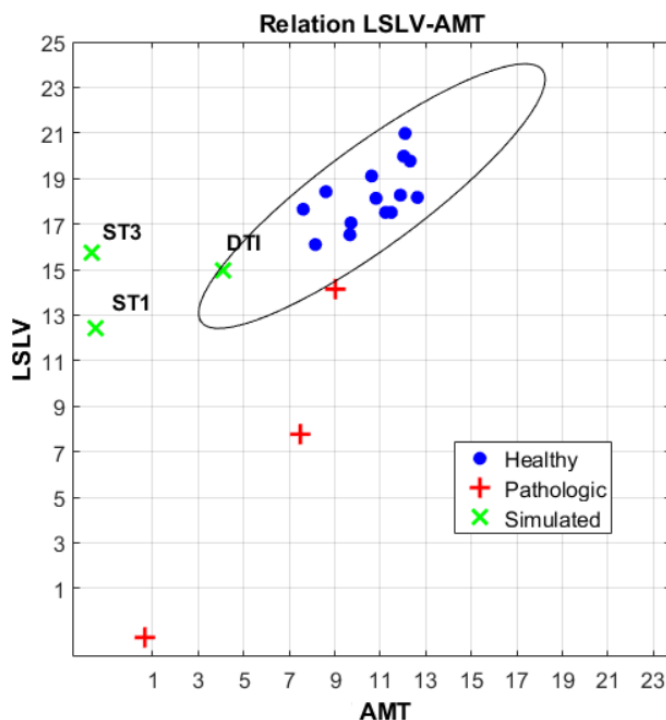
Fig. 8 Distribution of the pair (AMT, LVLS).

The helicoidal disposition generates SA rotations with opposite directions at basal and apical cuts that produce AMT [3]. Since Streeter fibers are defined according to a transition angle between endocardium and epicardium, rotations are equal at all SA cuts and, thus, AMT is not within normality ranges (fig.8). Basal connectivity induces a longitudinal shortening along the long axis direction. The lack of such connectivity in Streeter models introduces an anomalous folding (fig.6) of the septal basal region. This is not the case of DTI simulations, which shortening is along the long axis direction as expected in a healthy heart.

Even using a geometry extracted to preserve basal connectivity, the realism of DTI simulations at basal level is significantly worse (SA rotation). This might be attributed to the fact that blood inside the cavities was not considered and no wall force was imposed in the endocardium, neither pressure nor viscous strains.

Lack of blood flow might be considered a limitation, although our goal was to explore the influence of fiber connectivity to determine what assumptions should consider rule- based models. Our experiments show that models should consider the overall 3D connectivity of the muscular architecture. In order to model blood flow, geometries should be closed and include atria. This is a limitation for using DTI studies since atria fibers and tissue can not be

properly captured. In this context, modern techniques like synchrotron-based micro computed tomography [8] could be considered to obtain models including microstructure of the heart. Another limitation of this study is the use of a single geometry in simulations. This limits the predictive power of statistical models and further studies are needed to assess the precise impact of fiber connectivity and basal architecture.

In conclusion, our experiments show that simulations computed using experimental fibers achieve more realistic results and indicate that fiber connectivity at the basal loop could influence biomechanics. To firmly confirm this we plan to repeat this work using models with blood flow on the whole JHU dataset including pathological cases. Given the complexity of computations, such study is only feasible in a reasonable time using a HPC platform like Alya on the Marenostrum supercomputer.

Compliance with ethical standards

Conflict of Interest The authors declare that they have no conflict of interest.

Ethical approval For this type of study formal consent is not required

Informed consent This articles does not contain patient data

References

1. Bishop, M., Hales, P., Plank, G., Gavaghan, D.J., Scheider, J., Grau, V.: Comparison of rule-based and dtmri-derived fibre architecture in a whole rat ventricular computational model. In: Functional Imaging and Modeling of the Heart, pp. 87–96 (2009)
2. Carapella, V., Bordas, R., Pathmanathan, P., Lohezic, M., Schneider, J.E., Kohl, P., Burrage, K., Grau, V.: Quantitative study of the effect of tissue microstructure on contraction in a computational model of rat left ventricle. PloS one (2014)
3. Carreras, F., Garcia, J., Gil, D., Pujadas, S., Li, C.H., Suarez-Arias, R., Leta, R., Alomar, X., Ballester, M., Pons-Llado, G.: Left ventricular torsion and longitudinal shortening: two fundamental components of myocardial mechanics assessed by tagged cine-mri in normal subjects. Int J Card Imag **28(2)**, 273–84 (2012)
4. Casero, R., Burton, R.A., Quinn, T.A., Bollensdorff, C., Hales, P., Schneider, J., Kohl, P., Grau, V.: Cardiac valve annulus manual segmentation using computer assisted visualfeedback in three-dimensional image data. In: EMBC, pp. 738–741 (2010)
5. Ferreira, P.F., Kilner, P.J., McGill, L.A., Nielles-Vallespin, S., D Scott, A., Ho, S.Y., P McCarthy, K., Haba, M., Ismail, T., Gatehouse, P., Silva, R., Lyon, A., Prasad, S., Firmin, D.: In vivo cardiovascular magnetic resonance diffusion tensor imaging shows evidence of abnormal myocardial laminar orientations and mobility in hypertrophic cardiomyopathy. J Cardiovascular Mag Res **16 (87)**, 1–16 (2014)
6. Fritz, T., Wieners, C., Seemann, G.: Simulation of the contraction of the ventricles in a human heart model including atria and pericardium. Biomechanics and Modeling in Mechanobiology (13), 627â641 (2014)
7. Gil, D., Borras, A., Aris, R., Vazquez, M., Lafortune, P., Houzeaux, G., Aguado, J., Ballester, M., Li, C.H., Carreras, F.: What a difference in biomechanics cardiac fiber makes. In: STACOM (2012)

8. Gonzalez Tendero, A., Zhang, C., Balicevic, V., Cardenes, R., Loncaric, S., Butakoff, C., Paun, B., Bonnin, A., Garcia-Canadilla, P., Munoz-Moreno, E Gratacos, E., Crispi, F., Bijnens: Whole heart detailed and quantitative anatomy,myofibre structure and vasculature from x-ray phase-contrast synchrotron radiation-based micro computed tomography. EHJ-Cardio Imag **18**, 732–41 (2017)

9. Gurev, V., Lee, T., Constantino, J., Arevalo, H., Trayanova, N.A.: Models of cardiac electromechanics based on individual hearts imaging data. Biomech Mod Mechanobiology **10(3)**, 295–306 (2011)

10. Helm, P.A., Younes, L., Beg, M.F., Ennis, D.B., Leclercq, C., Faris, O.P., McVeigh, E., Kass, D., Miller, M.I., Winslow, R.L.: Evidence of structural remodeling in the dyssynchronous failing heart. Circulation Research **98**(1), 125–132 (2006)

11. Humphrey, J.: Cardiovascular solid mechanics. cells, tissues, and organs. Springer (2001)

12. Hunter, P.J., McCulloch, A.D., ter Keurs, H.E.: Modelling the mechanical properties of cardiac muscle. Prog. Biophys. Mol. Biol. **69**(2-3), 289–331 (1998)

13. Lafortune, P., Arís, R., Vázquez, M., Houzeaux, G.: Coupled electromechanical model of the heart: Parallel finite element formulation. International Journal for Numerical Methods in Biomedical Engineering **28**, 72–86 (2012)

14. Myerburg, R.J., Nilsson, K., Gelband, H.: Physiology of canine intraventricular conduction and endocardial excitation. Circ Res **30**(2), 217–243 (1972)

15. O'Hara, T., Virag, L., Varro, A., Rudy, Y.: Simulation of the undiseased human cardiac ventricular action potential: model formulation and experimental validation. PLoS Comput. Biol. **7**(5) (2011)

16. Potse, M., Dube, B., Richer, J., Vinet, A., Gulrajani, R.M.: A comparison of monodomain and bidomain reaction-diffusion models for actionpotential propagation in the human heart. Trans. Biomed Eng **53 (12)**, 2425–2435 (2006)

17. Poveda, F., Gil, D., Marti, E., Andaluz, A., Ballester, M., Carreras, F.: Helical structure of the cardiac ventricular anatomy assessed by diffusion tensor magnetic resonance imaging multi-resolution tractography. Rev Esp Card **66(10)**, 782–90 (2013)

18. Santiago, A.: Fluid Electro Mechanical model of the human heart for supercomputers. PhD Thesis. UPC, Barcelona, Spain (2018)

19. Savadjieva, P., Strijkers, G.J., Bakermans, A.J., Piuze, E., Zucker, S., Siddiqi, K.: Heart wall myofibers are arranged in minimal surfaces to optimize organ function. PNAS **109(24)** (2012)

20. Scollan, D., Holmes, A., Winslow, R., Forder, J.: Histological validation of myocardial microstructure obtained from diffusion tensor magnetic resonance imaging. American Journal of Physiology **275**, 2308–2318 (1998)

21. Sebastián, R., Zimmerman, V., Romero, D., Sánchez-Quintana, D., Frangi, A.F.: Characterization and modeling of the peripheral cardiac conduction system. IEEE Trans Med Imaging **32**(1), 45–55 (2013)

22. Streeter, D., Spotnitz, H., Patel, D., Ross, J., Sonnenblick, E.: Fiber orientation in the canine left ventricle during diastole and systole. Circulation Research **24**, 339–347 (1969)

23. Teh, I., McClymont, D., Burton, R., Maguire, M., Whittington, H., Lygate, C., Kohl, P., Schneider, J.: Resolving fine cardiac structures in rats with high-resolution dti. Nature-Sci Reports **6:30573**, 1–14 (2016)

24. Torrent Guasp, F., Ballester, M., Buckberg, G., et al.: Spatial orientation of the ventricular muscle band: physiologic contribution and surgical implications. J Thorac Cardiovasc Surg **122(2)**, 389–92 (2001)

25. Toussaint, N., Stoeck, C., Schaeffter, T., Kozerke, S., Sermesant, M., Batchelor, P.: In vivo human cardiac fibre architecture estimation using shape-based diffusion tensor processing. Medical Image Analysis **17**, 1243–1255 (2013)

26. Vázquez, M., Arís, R., Aguado-Sierra, J., Houzeaux, G., Santiago, A., López, M., Córdoba, P., Rivero, M., Cajas, J.C.: Alya red ccm: Hpc-based cardiac computational modeling. Selected Topics of Computational and Experimental Fluid Mechanics pp. 189–207 (2015)